Modeling the Corrosion of Steel Casing and the Damage of Well Cement in a Borehole System

Linfei Li[a], Mija H. Hubler[a], Yunping Xi[a,*]

[a] University of Colorado, Department of Civil and Environmental Engineering, Boulder, CO 80309, USA
[*] Corresponding author.
E-mail address: yunping.xi@colorado.edu (Xi, Y.).

Abstract: This paper presents the effect of chloride-induced corrosion in an underground borehole system, specifically considering the steel casing and further damage to the surrounding cement. In the past four decades, oil well cement has been successfully used for underground construction. However, high concentrations of chloride ions gradually degrade the functionality and durability of well cement. Gasses and liquids can leak from deterioration caused by chloride ions, and thus motivate this study. The chemo-mechanical coupling diffusion model and a classical fracture mechanics model are applied. The model is validated with OPC concrete corrosion data from literature, and then applied to well cement using experimentally obtained material property data. The time when crack initiation, peak pressure, and complete fracture is reached in the model of the cement sheath provides a quantification of the expected service life of the borehole system.

Keywords: Well cement, Chloride diffusion, Corrosion, Crack propagation

1 Introduction

In the last forty years, corrosion of steel embedded in concrete has become one of the most critical problems of the durability of reinforced concrete structures [1]. Based on a study from National Association of Corrosion Engineers (NACE), the estimated annual cost of repairing corrosion related damages is $276 billion in the United States [2]. One of the main causes for the corrosion of steel is the intrusion of chloride ions into concrete [3]. In chloride-induced corrosion, the chloride ions in the pore solution of the concrete can form electrolytes enable the onset of steel corrosion [4].

Steel casings used in the oil and gas industry are embedded in well cement in a borehole system. They are exposed to subsurface water with high chloride concentrations and are therefore vulnerable to corrosion damage. In this paper, the chloride-induced corrosion of steel casings used in underground borehole systems is the studied since it can degrade the service life of the system [5].

1.1 Chloride Corrosion Mechanism

There are three stages in the deterioration process of the corrosion of steel in cementitious materials due to the intrusion of chloride ions: the first one is the chloride penetration into concrete; the second is the rust formation and accumulation at the interface between the steel and concrete; and the third is crack development in the surrounding cementitious materials. Once the corrosion process has begun, it is irreversible. It is therefore important to characterize the penetration process of chloride into the surrounding cementitious materials. Since the volume of rust is much larger than the volume of the steel, there will be a pressure generated at the steel/cement paste interface, and the pressure will increase as the corrosion progresses. When the

pressure is beyond the tensile strength of the surrounding cementitious material, the cement paste cover will start to crack.

The penetration period of chloride ions is the largest and most significant factor that needs to be considered for aboveground structures. Chloride ions penetrate through the surrounding concrete to the outer surface of the rebar. Once the concentration of chloride ions exceeds a critical value, the chloride ions will destroy the passive film on the surface of the steel, which is the steel's final defense against corrosion. According to a previous study in Colorado, U.S., most this process usually takes 7-20 years in above ground reinforced concrete structures [6], depending on the quality of concrete and the service environment [7]. The rate of chloride penetration into the concrete mainly depends on the pore structure of the concrete. The pore structure of concrete is influenced by several factors, such as the type of cement used, aggregate properties, mixing procedure, curing procedure, and the age of the concrete. Mix design factors such as the water-to-cement ratio, mixing time, and additives also influence the pore structure [8]. From previous research, concrete cured at room temperature will hydrate better which means the diffusion coefficient of chloride into the concrete will be lower. Curing at high temperatures will generate an accelerated curing process, which can cause a more resistant concrete in the early stages. However, with the accelerated curing process, the concrete will not have enough time to hydrate, which causes an increase in porosity and results in a higher diffusion coefficient for chloride [9].

The steel casings used in the oil and gas industry are in a similar environment as embedded steel bars in reinforced concrete structures. The difference is that the steel casings are surrounded by well cement paste, while steel bars are surrounded by concrete cover. The average concrete cover for structures above ground is about two inches (five centimeters), similar to the thickness of the well cement paste surrounding a steel casing. The chloride-induced corrosion mechanisms for both cases are the same. For a borehole system, the chloride ions penetrate from the surrounding well cement to the embedded steel casing. Once the corrosion starts, the corrosion of steel will generate rust products at the interface between the steel and the surrounding well cement. For aboveground structures, all three stages of the chloride corrosion mechanism are important. For underground structures, the first stage is much shorter than that in aboveground structures because of the high moisture levels and high chloride concentrations in subsurface water which can generate a high rate of the production of rust from the steel pipe. Therefore, in this specific case, the chloride profile may not be the governing feature of the corrosion process. There are many models developed for the first stage already [10-12]. Based on the underground environment, this study's focus is on the second and the third stage. The rust generation will be considered as the beginning of the corrosion damage process.

1.2 The corrosion of steel casing in boreholes

Figure 1 shows the side view and top view of a borehole system. The steel pipe is installed first, then the well cement is injected though the steel pipe and hardens around the outside of it. The corrosion of the steel will start from the outer surface of the steel pipe, and rust will be generated and deposit on the outer surface of the pipe. The volume expansion of the rust layer generates circumferential tensile stress, which can crack the well cement. At the same time, the thickness of the steel pipe is reduced due to the formation of rust. Therefore, the strength of the steel pipe and the well cement degrade due to the corrosion process [5].

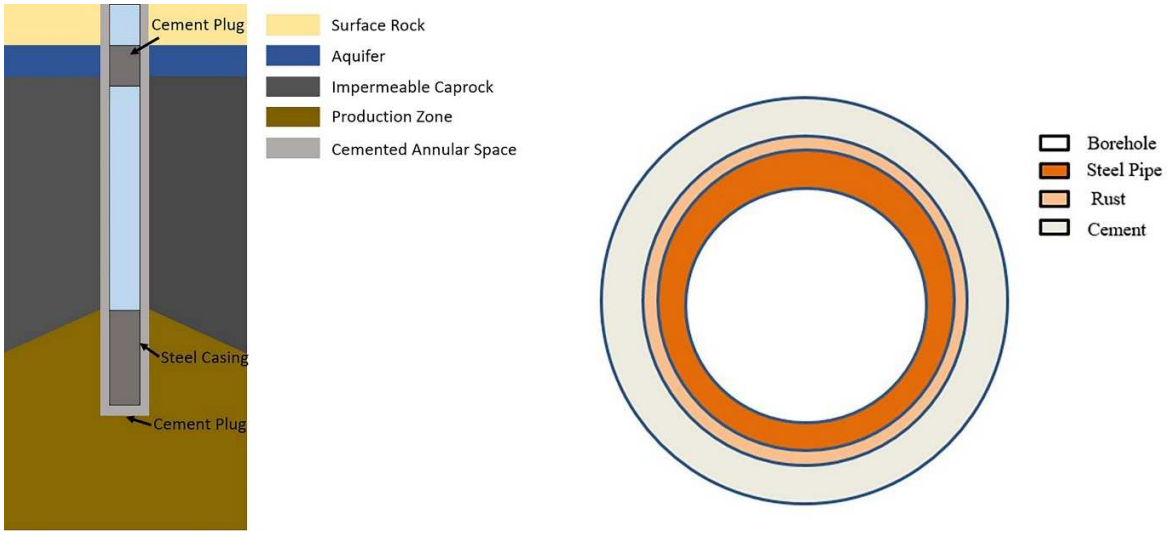

Figure 1. Well Borehole System (a) Side View (b) Top View (Cross Section)

Once the rust production starts, it will first fill the interface transition zone (ITZ) which is between the steel and surrounding well cement and the space left from the corroded steel. This generates no pressure in on the cement. This stage depends highly on the corrosion rate and the porosity of the ITZ. After the ITZ and volume of corroded steel is filled, the rust will start to generate pressure on the interface, which will push the rust into the surrounding cementitious material. As rust production continues, the pressure at the inner surface of the cement will keep increasing [11]. Similarly, the tangential stress acting in the circumferential direction will also increase with the increase of pressure. After several months (or years) of rust accumulation, the tangential stress will eventually be higher than the tensile strength of the cementitious material. Therefore, the rust accumulation and the tensile strength of the cement will dictate when cracking initiates in the cement. The cracked material has a lower resistance to crack propagation than the intact well cement. Therefore, once the cement cracks the system will rapidly degrade. To simulate the crack propagation, fracture mechanics is applied. A flow chart of the deterioration process is shown in Figure 2.

Figure 2. Procedure of Cement from Intact to Failure

Generally, three phases can be described: the rust production period, the pressure build up period (or accumulate period), and the crack propagation period. These are shown in Equation 1. In literature, there are other phase-separated methods which have been provided by other authors, such as Tuutti, who only split the process into two phases: "initiation" and "propagation" [13-15].

$$T_{service} = T_{rust} + T_{stimulate} + T_{crack} \qquad (1)$$

1.3 Motivation of Work

The objective of this work is to use a chemo-mechanical coupled model to simulate and predict the performance of cementitious material underground surrounding steel casing in a borehole. The chloride ions come from subsurface water. The high porosity of oil well cement,

discovered to be approximately 40% in previous research [16], leads to a lower resistance to the penetration of rust in well cement than that of regular Portland cement concrete. The pressure, temperature, and moisture levels underground are all higher than those above ground. Therefore, the penetration rate of chloride is higher. For this study, therefore, we focus on the corrosion process since the duration of the chloride diffusion process is significantly shorter.

Our literature review indicated that there is no existing model to predict the fracture properties of oil well cement underground due to the corrosion of steel. Most of the previous work was focused on structures under atmospheric conditions, especially for reinforced concrete structures above ground [6-11]. Therefore, a new model needs to be developed based on previous work with major modifications to take into account the underground conditions in well cement.

2 Procedure of Modelling Work

2.1 Rust Production Period

Once the corrosion process of steel starts, it can be assumed that the chloride content, moisture, and oxygen will be at sufficient levels for the continuation of the corrosion process. The discontinuation of these influential factors will decrease the corrosion rate, but it is assumed the subsurface environment will provide a continuing supply. The mass of the steel loss during the corrosion process can be obtained by using Faraday's law, shown in Equation 2. The rate of steel loss can then be determined by dividing Equation 2 with time, which is shown in Equation 3. The depth of corrosion per unit area can then be calculated by dividing Equation 3 by the density of the steel, shown in Equation 4.

$$m_s = \frac{a_s}{nF} i_{corr} t \qquad (2)$$

$$\mu = \frac{m_s}{t} = \frac{a_s}{nF} i_{corr} \qquad (3)$$

$$d = \frac{a_s}{nF\rho_s} i_{corr} t \qquad (4)$$

where a_s is the atomic mass for steel, n is the equivalents exchanged, F is the Faraday's constant, i_{corr} is the annual mean corrosion density, t is the time, μ is the rate of steel loss, ρ_s is the density of steel, and d is the depth of corrosion per unit area. Table 1 shows the values of constants used in the calculation. A similar value of i_{corr} has been used in the previous research [17-19].

Table 1 Corrosion Parameters.

i_{corr} $(\mu A/cm^2)$	n	a_s (g/mol)	F (C/mol)	ρ_s (g/cm^3)
1	2	55.85	96500	7.87

When the depth of corrosion into the steel has been obtained, the next step is to calculate the volume of corrosion product as a ring with an inner radius R_i of cement annulus. The equation is shown below:

$$V_{rust} = \alpha\pi(2R_i d - d^2) \qquad (5)$$

where α is the volume ratio of the corrosion product to the corroded steel pipe. The value of α mainly depends on the chemical composition of the rust, which is shown in Table 2 [11].

Table 2 Chemical Composition of Rust.

Corrosion Product	Volume Ratio
FeO	1.7
Fe_3O_4	2
Fe_2O_3	2.1
$Fe(OH)_2$	3.6

From the above equations, the total rust generation as a function of time can be obtained. However, not all the rust produced will cause increased pressure and permeate into the cementitious material. As discussed in the previous section, there is a porous zone between the steel pipe and surrounding cement matrix, named interface transition zone (ITZ) [20]. The corrosion product will first fill the space left by the corroded steel, and then move into the ITZ. The rust stored in these two places will not generate any pressure. Therefore, the volume of rust in the corroded steel and ITZ must be subtracted from the total volume of rust generated, Equation. 6.

$$V_{eff} = V_{rust} - V_{ITZ} - V_{cs} \qquad (6)$$

where V_{ITZ} is the volume of ITZ, V_{cs} is the volume of corroded steel, V_{eff} is the volume of rust which can generate pressure and further permeate into the cement matrix.

$$V_{cs} = \frac{V_{rust}}{\alpha} \qquad (7)$$

$$V_{ITZ} = d_{ITZ} A_{Steel} \qquad (8)$$

$$d_{ITZ} = h_i \varphi_i \qquad (9)$$

where h_i is the thickness of ITZ, φ_i is the porosity of ITZ, d_{ITZ} is the volume of the porous zone which can absorb the rust per unit area, A_{steel} is the surface area of steel pipe.

When the value of V_{eff} is larger than zero, it means that the spaces left by the corroded steel and the ITZ pores have been filled with rust. Once these spaces are full, the rust will start penetrating the surrounding cement matrix. This diffusion process can be simulated using Darcy's law, Equation 10.

$$\frac{\partial C_{rust}}{\partial t} = \nabla\left(\frac{\kappa_{rust}}{\eta_{rust}} \nabla P_{rust}\right) \qquad (10)$$

where C_{rust} is the concentration of rust in pores, κ_{rust} is the viscosity of rust, η_{rust} is the rust diffusivity, and P_{rust} is the pressure distribution based on the concentration of rust, which heavily rely on the degree of rust concentration.

From the equations above, one can see that to solve this chemo-mechanical coupled diffusion equation, another equation to connect C_{rust} to P_{rust} is necessary. Therefore, a simple linear state equation is provided below:

$$C_{rust} = \beta P_{rust} \qquad (11)$$

where β is a state function, which can be determined by the process of penetration, C_p and f_t are the porosity and tensile strength of cement matrix. When all the porous media in the cement matrix are filled, $C_{rust} = C_p$. At the same time, $P_{rust} = f_t$. Any additional rust generation causes a pressure build-up in the cement. The pressure generated from the rust may be larger than the tensile strength of the cement, causing cracking.

So, one can conclude that:

$$\beta = \frac{C_p}{f_t} \qquad (12)$$

Combining Equations 10 to 12, and the diffusion equation can then be revised as:

$$\frac{\partial C_{rust}}{\partial t} = k\left(\frac{\partial^2 C_{rust}}{\partial^2 r} + \frac{1}{r}\frac{\partial C_{rust}}{\partial r}\right) \qquad (13)$$

where r is the radius of the surrounding cement.

$$k = \frac{f_t \kappa_{rust}}{C_p \eta_{rust}} \qquad (14)$$

Table 3 Parameters Used in the Diffusion Equation [11].

f_t (Mpa)	C_p (%)	$\frac{\kappa_{rust}}{\eta_{rust}}$
3.3	40	0.00058

The boundary condition (*B.C.*) and initial condition (*I.C.*) of this diffusion equation is shown in the equations below:

$$I.\,C.:\ C_{rust}(r,0) = 0 \qquad (15)$$

$$B.\,C.:\ C_{rust}(R_i,t) = \beta P_{int}(t) \qquad (16)$$

$$B.C.:\ C_{rust}(R_0,t) = 0 \qquad (17)$$

where R_i is the inner radius of the cement, which equals the radius of steel pipe, and R_o is the outer radius of the cement around the pipe.

Initially, the concentration of rust in cement pores would be zero on the boundary. When the diffusion process begins, the concentration of rust at the interface between steel pipe and cement surrounding is found using Equation 16. The system can be treated as a thick-wall cylinder, where R_0 is a point far away from the outer surface of the steel casing. The only unknown value is the $P_{int}(t)$, which is the pressure at the interface between steel casing and cement matrix. As there is no expression for $P_{int}(t)$, this can be figured out by using a numerical method, such as a finite difference method. In this paper, Euler-backward discretization on radial direction has been applied. The details are shown in the equations below:

$$\frac{C_j^{n+1} - C_j^n}{\Delta t} = k\left(\frac{1}{r_j}\frac{C_{j+1}^{n+1} - C_{j-1}^{n+1}}{2\Delta r} + \frac{C_{j+1}^{n+1} - 2C_j^{n+1} + C_{j-1}^{n+1}}{\Delta r^2}\right) \qquad (18)$$

$$\text{For j=1:}\ \ C_1^{n+1} = \beta P_{int}(t) \qquad (19)$$

$$\text{For j=2:J-1:}\ \ -k\left(\frac{\Delta t}{2r_j\Delta r} + \frac{\Delta t}{\Delta r^2}\right)C_{j+1}^{n+1} + \left(1 + \frac{2\Delta t k}{\Delta r^2}\right)C_j^{n+1} + k\left(\frac{\Delta t}{2r_j\Delta r} - \frac{\Delta t}{\Delta r^2}\right)C_{j-1}^{n+1} = C_j^n \qquad (20)$$

$$\text{For j=J:}\ \ C_J^{n+1} = 0 \qquad (21)$$

From Equation 18 to 21, the diffusion equation has been discretized in time by *n*, and in space by *j*. Then, it can be formed as a tridiagonal matrix and solved using the Thomas algorithm.

The next step is to calculate the volume of rust penetrated in the cement matrix at each time step. This can be accomplished by integrating the concentration of rust product in the cement matrix over the total volume of the surrounding cement matrix:

$$V_{rust}^{cement} = \int_{R_i}^{R_o} 2\pi r C_{rust}\, dr \qquad (22)$$

It is important to note that the total volume of rust production is divided into several parts: the rust which has filled some of the cement pores, the rust stored in the ITZ, the rust stored in the space of the corroded steel, and the rust that will cause the expansion and further create the crack on the cement surrounding. The volume of the rust which causes the expansion of cement is denoted as ΔV_{rust}, and it can be calculated with Equation 23. Finally, the radial expansion of the cement surrounding can be directly derived from Equation 24.

$$\Delta V_{rust} = V_{eff} - V_{rust}^{cement} \quad (23)$$

$$\delta_{R_i} = \sqrt{\frac{\Delta V_{rust} + \pi R_i^2}{\pi}} - R_i \quad (24)$$

where δ_{R_i} is the radial expansion due to the interface pressure at R_i.

2.2 Pressure Build-up Period

The total volume of the rust generated is much larger than the volume of the rust stored in the cement matrix. ΔV_{rust} generates interface pressure as shown in Figure 3. Therefore, this problem can be treated as a hollow thick wall cylinder problem with hydrostatic pressure at each time period. When the pressure level is low, the interface pressure will not generate any cracks on the surrounding cement. A linear elastic condition for the thick wall cylinder can hence be considered, and the relationship between radial expansion and the interface pressure can be developed. This problem can be solved by using the Timoshenko solution [21] for a thick-walled cylinder. First, the stresses in different directions on the hollow thick wall can be calculated using Equations 25 to 27.

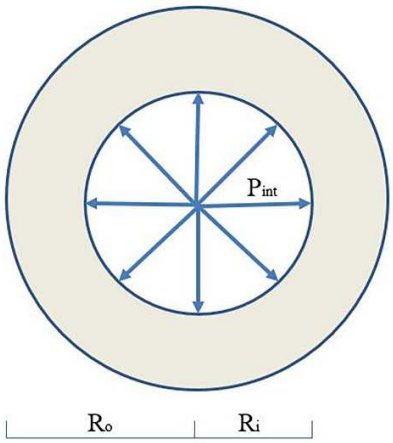

Figure 3. The Thick-Wall Problem for Simulating the Cement due to the Rust

$$\sigma_{rr}(r) = \frac{PR_i^2}{R_0^2 - R_i^2}\left(1 - \frac{R_0^2}{r^2}\right) \quad (25)$$

$$\sigma_{\theta\theta}(r) = \frac{PR_i^2}{R_0^2 - R_i^2}\left(1 + \frac{R_0^2}{r^2}\right) \quad (26)$$

$$\sigma_{r\theta} = 0 \quad (27)$$

where σ_{rr} is the stress in the radial direction, and $\sigma_{\theta\theta}$ is the stress in the tangential direction.

The next step is to build the connection between tangential stress and radial displacement at R_i, which is shown in Equation 28. Finally, after combining Equations 26 and 28, the linear elastic solution for calculating the interface pressure can be obtained from the product, Equation 29.

$$\delta_{R_i} = \frac{R_i}{E}\sigma_{\theta\theta}(R_i) \quad (28)$$

$$P_{int} = \frac{E}{R_i}\frac{R_0^2 - R_i^2}{R_0^2 + R_i^2}\delta_{R_i} \quad (29)$$

Based on the equations above, the interface pressure before crack formation in well cement can be calculated using linear elasticity. With the penetration of the rust, the interface pressure will continually increase until it reaches a critical value for the onset of cracks in well cement.

2.3 Crack Propagation Period

When the tangential stress generated by the pressure build-up at the inner radius is larger than the tensile strength of the surrounding cement, nonlinear fracture mechanics must be used to calculate the interface pressure. In previous research, several nonlinear fracture models have been developed, such as size effect law and the fictitious crack model [22-24]. In the last two decades, more similar nonlinear fracture models have also been developed [25-27]. In this work, the Fictitious Crack Model will be adopted for calculating the pressure change after interface cracks develop.

The objective of using this model is first to build a relationship between the crack size and radial expansion, and further derive the pressure generated from the radial displacement. The fictitious crack model assumes that cracks will appear when the pressure is higher than the tensile strength of the cementitious material. With a continuous increase of the crack size, the tangential stress will decrease with time. When the crack size reaches a critical value, the stress will decrease to zero. Generally, the relationship between tangential stress and crack size needs to be obtained from experimental work. In this study, this relationship was simplified as a linear function as shown in Figure 4 [11]. From the figure below, one can see that when the tangential stress is equal to the tensile stress of the cement, there are no cracks. During the crack propagation process, when the critical crack size (w_c) is reached, the tangential stress equals zero. Equation 30 describes this process. The area in the figure below the curve is the total energy absorbed during the full process of the fracture propagation, which can be calculated with Equation 31. Combining Equations 30 and 31, produces the expression of critical crack length that can be calculated in Equation 32. In addition, the fracture energy for the oil well cement may be tested by doing a three-point-bending test.

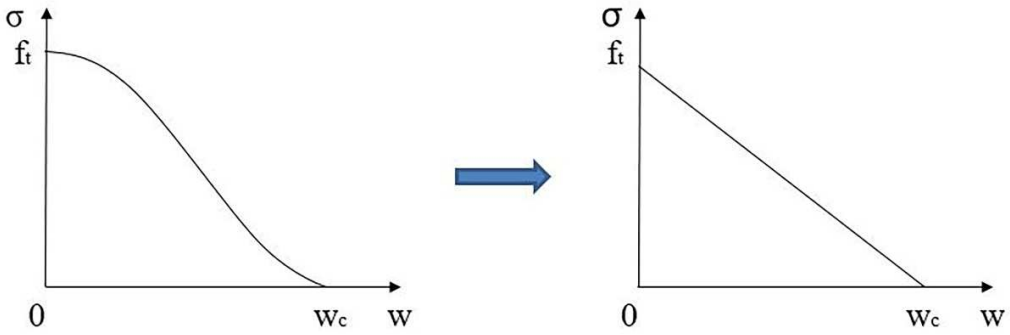

Figure 4. The Relationship between Tangential Stress and Crack Size

$$\sigma(w) = f_t(1 - \frac{w}{w_c}) \qquad (30)$$

$$G_c = \int_0^{w_c} \sigma(w)dw \qquad (31)$$

$$w_c = 2\frac{G_c}{f_t} \qquad (32)$$

In the fictitious crack model, the surrounding cement after the crack formation can be divided into two parts: the linear elastic part (uncracked section) and the softening part (cracked

section). Both parts will provide resistance to cracking. The energy balance equation can be seen in Equation 33.

$$2P_{int}R_i = 2P_{cr}R_{cr} + 2\int_{R_i}^{R_{cr}} \sigma_{\theta\theta}(r)dr \qquad (33)$$

where P_{cr} is the resistance from the elastic part, R_{cr} is the critical radius that separates the elastic and softening parts, and the second part on the right-hand side is the resistance from the cracked section (integral part).

In Equation 33, there is a constant '2' on both sides of the equation. This is due to the symmetry of the stress field in consideration. When a cut is made in a horizontal direction on the wellbore hole, two cracks are assumed in opposing directions, which is shown in Figure 5. It should be mentioned that different numbers of cracks will not affect the form of Equation 33. The only change is to replace "2" by "n". The value of P_{cr} can be calculated based on the elastic solution, in Equation 34. The critical radius will be calculated based on the radial displacement at R_i (Equation 35).

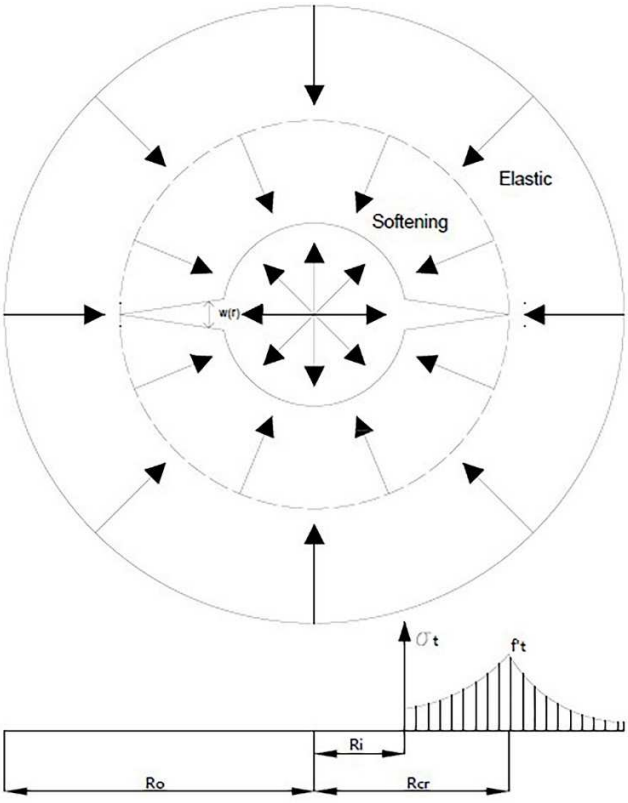

Figure 5. Equilibrium of the stress relations due to the rust production

$$P_{cr} = f_t \frac{(R_o^2 - R_{cr}^2)}{(R_o^2 + R_{cr}^2)} \qquad (34)$$

$$R_{cr} = \frac{E}{f_t}\delta_{R_i} \qquad (35)$$

Then, the only unknown variable is tangential stress ($\sigma_{\theta\theta}(r)$). To formulate the tangential stress, first the tangential elongation will be considered. From Figure 5, the total tangential

elongation includes two parts: the elongation from elastic part and the width of the two cracks. Therefore, the elongation can be obtained using Equation 36.

$$e(r) = 2w(r) + (2\pi r - 2w(r))\varepsilon_t(r) \qquad (36)$$

where ε_t is the tangential strain.

Since the value of $2w(r)\varepsilon_t(r)$ is much smaller than the value of $2\pi r\varepsilon_t(r)$, it can be neglected from the calculation, which means Equation 36 can be simplified as in Equation 37.

$$e(r) = 2w(r) + 2\pi r\varepsilon_t(r) \qquad (37)$$

When the radius r reaches the critical radius R_{cr}, the tangential stress of the cement would be equal to the tensile strength of the cement matrix. Therefore, the crack width at the critical radius R_{cr} equals zero. Poisson's effect has been neglected. Using Equations 37 to 39, the equation of crack width can be derived. Finally, after combining Equations 40 and 32, the general expression of tangential stress due to the radius can be obtained in Equation 41.

$$e(R_{cr}) = 2\pi R_{cr}\varepsilon_{cr} \qquad (38)$$

$$\varepsilon_{cr} = \frac{f_t}{E_c} \qquad (39)$$

$$w = \pi\left(R_{cr}\frac{f_t}{E_c} - r\varepsilon_t(r)\right) = \pi\left(R_{cr}\frac{f_t}{E_c} - r\frac{\sigma_t(r)}{E_c}\right) \qquad (40)$$

$$\sigma_t(r) = f_t\left(\frac{2EG_c - \pi R_{cr}f_t^2}{2EG_c - \pi r f_t^2}\right) \qquad (41)$$

Combining the derived Equations 33-41, the expression of interface pressure P_{int} can be obtained:

$$P_{int} = f_t\frac{(R_o^2 - R_{cr}^2)}{(R_o^2 + R_{cr}^2)}\frac{R_{cr}}{R_i} + \frac{1}{R_i}\int_{R_i}^{R_{cr}} f_t\left(\frac{2EG_c - \pi R_{cr}f_t^2}{2EG_c - \pi r f_t^2}\right)dr \qquad (42)$$

This equation can be numerically solved:

$$P_{int} = f_t\frac{(R_o^2 - R_{cr}^2)}{(R_o^2 + R_{cr}^2)}\frac{R_{cr}}{R_i} + \frac{(\pi R_{cr}f_t^2 - 2EG_c)}{\pi R_i f_t}\ln\left(\frac{2EG_c - \pi R_{cr}f_t^2}{2EG_c - \pi R_i f_t^2}\right) \qquad (43)$$

Equation 43 calculates the interface pressure after a crack appears. One thing to note is that during the crack propagation, the chemical-mechanical coupling phenomenon still exists. The diffusion in Equation 14 always needs to be considered both in the uncracked step and in the cracking step. One can determine the interface pressure change by using theoretical analysis [28, 29].

3 Numerical Procedure

Since all the equations needed for the numerical procedure have been provided above, a brief discussion of the results will be provided. One thing to notice is that the inner side of the boundary condition varies with time, which means the assumed pressure in the boundary condition must be equal to the pressure calculated based on the theoretical analysis. Therefore, a finite difference method is introduced to solve this chemo-mechanical coupled problem.

The first step is to input all the corrosion product's parameters, such as the Young's modulus of the cementitious material, the annual mean corrosion density, and the size of the steel pipe and cement surroundings, etc. When all the parameters have been entered, the timestep needed for iteration will be determined. In this case, the simulation time is fixed at 0.01 years. The next step is to use the equations above to calculate the depth of corrosion in the steel pipe and iteratively calculate the ITZ pressure when the pores in the ITZ and corroded steel are filled with rust. After that, interface pressure will start to be generated. An assumed interface pressure is used to solve the diffusion equation. The rust distribution is obtained after the calculation. Based on the rust

distribution from the diffusion equation, one can obtain the volume expansion of the corrosion product and the radial displacement of the structure. Then, one calculates the interface pressure from the stress in the cement by using either the linear elastic method or nonlinear fracture mechanics which are determined by the stress in the cement surroundings. The last step is to make a comparison of the computed interface pressure with the assumed interface pressure. If there is a difference larger than the tolerance set, which equals 1×10^{-3} MPa, the calculation is re-run until the convergence is within the tolerance zone.

4 Model Validation Using Concrete

The results from the theoretical and numerical models need to be validated. The model prediction results are highly dependent on the input material parameters. With different parameters, such as the radius of the steel pipe, or the annual corrosion density, the crack propagation times are different. Based on previous research, some experimental results from a corrosion test of concrete can be used here for validation [30]. The experimental results are shown in Table 4.

Table 4 Adjusted Model Compared with the Experimental Study on First Cracking.

Case	*Ri* (*mm*)	R_o (*mm*)	*E* (*Mpa*)	f_t (*Mpa*)	i_{corr} ($\mu A/cm^2$)	T_{Ex}	T_{Model}
1	8	34.88	27000	3.3	3.75	0.72	0.67
2	8	56	27000	3.3	2.41	1.84	1.84
3	8	78.3	27000	3.3	1.79	3.54	3.54

where T_{Ex} is the time to first cracking, and T_{Model} is the time to the first crack predicted in the modelling work.

According to the test results and comparisons shown in Table 4, one can conclude that only the time to the first crack can be used to compare with the modelling work, which is the simulation results obtained from Section 2.1 and 2.2. The results from the model and the actual time to the first crack shown in Table 4 are close to the results from the experimental work, especially for case 2 and 3, which have large size of the concrete. The comparison is directly indicative of the effectiveness of the model.

Simulation of interface pressure and concentration of rust is shown in Figures 6 to 8. From part (a) of these figures, one can see that the interface pressure would increase with time before arriving at the peak value. The complete cracking time depends on the size of cement surrounding and the annual corrosion density. After the interface pressure passes the peak value, it drops rapidly to zero, which means the structure would crack quickly after reaching the peak load. From part (b) of these figures, the radial displacement, similarly, would increase with the increase of interface pressure before reaching the peak interface pressure. After reaching the peak pressure, the radial displacement would continuously increase with a lower rate. In part (c) of these figures, one can see that the concentration of rust is low compared with general chloride concentration [31]. The concentration of rust is influenced only by the diffusion coefficient of rust, "*k*" in Equation 14. In conclusion, although the entire process cannot be validated from the previous experimental study, the simulation of the behavior before cracking can be validated.

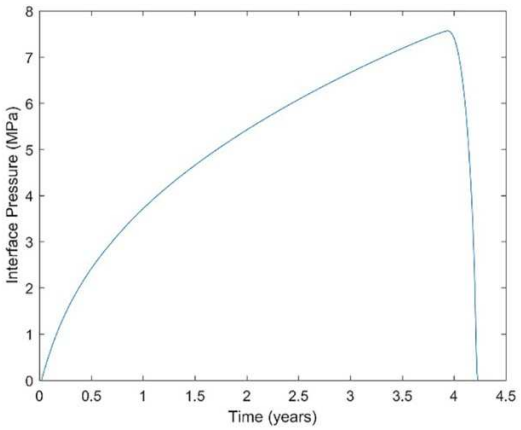

(a)

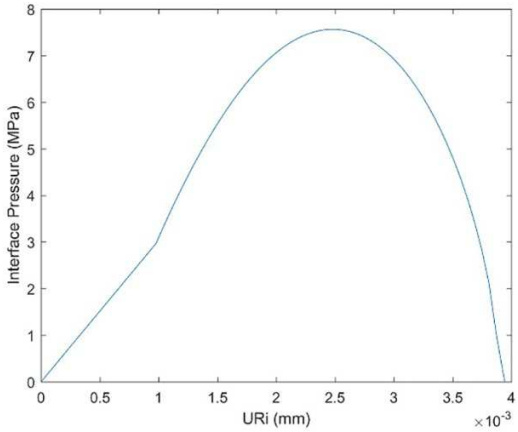

(b)

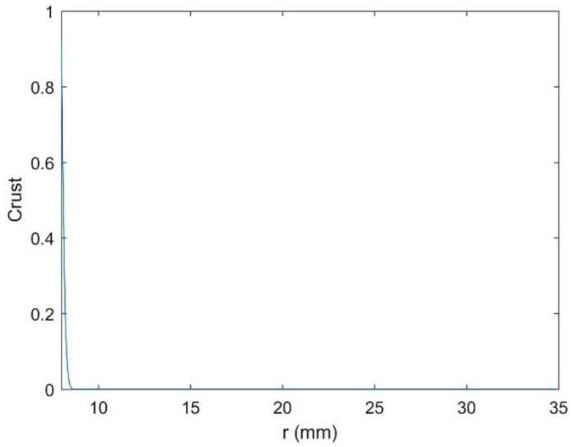

(c)

Figure 6. Modelling Results for Case 1 (a) Interface Pressure vs. Time (b) Interface Pressure vs. Radial Expansion of Concrete (c) Concentration of Rust along the Radius of Concrete

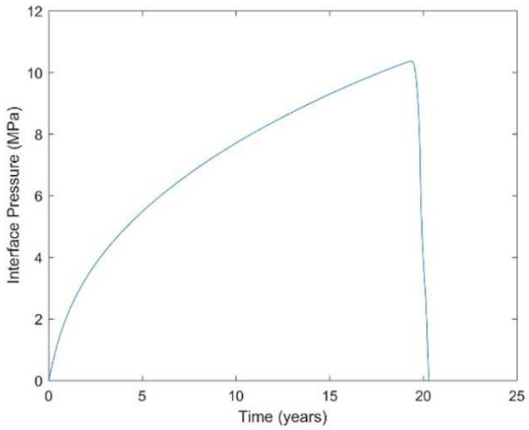

(a)

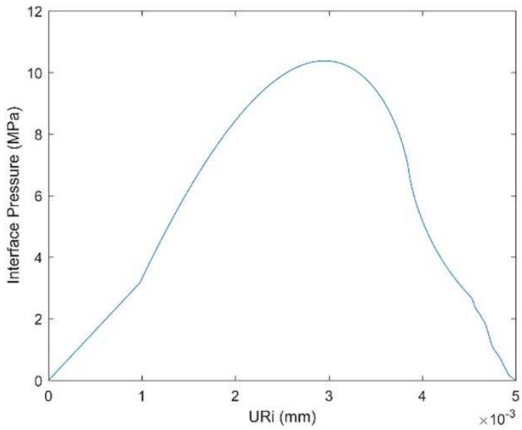

(b)

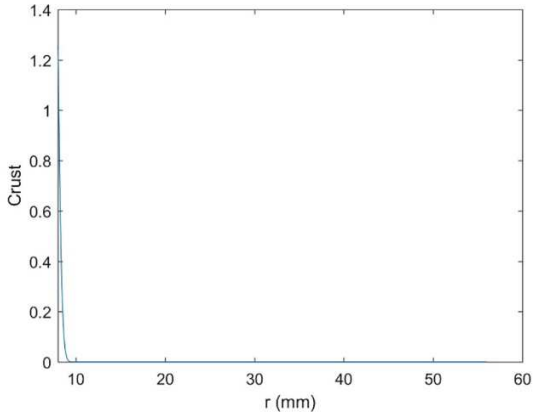

(c)

Figure 7. Modelling Results for Case 2 (a) Interface Pressure vs. Time (b) Interface Pressure vs. Radial Expansion of Concrete (c) **Concentration** of Rust along the Radius of Concrete

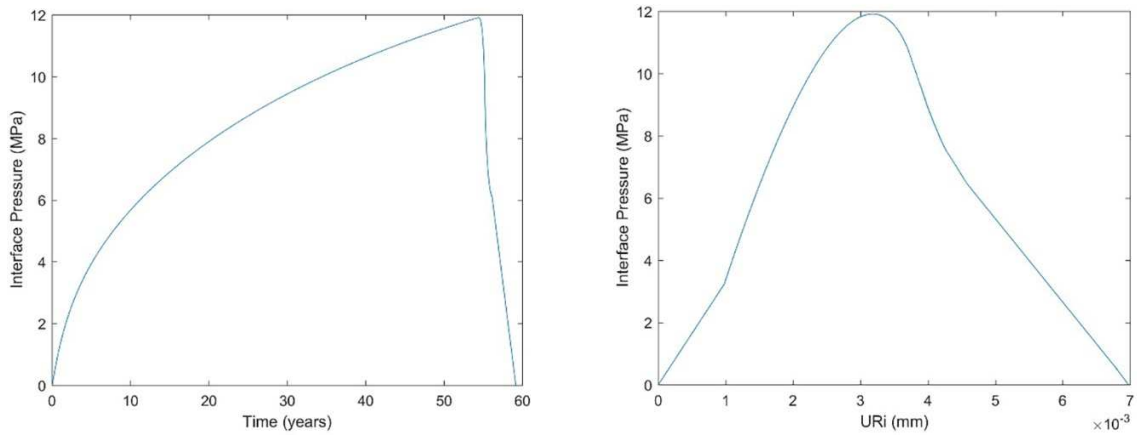

(a) (b)

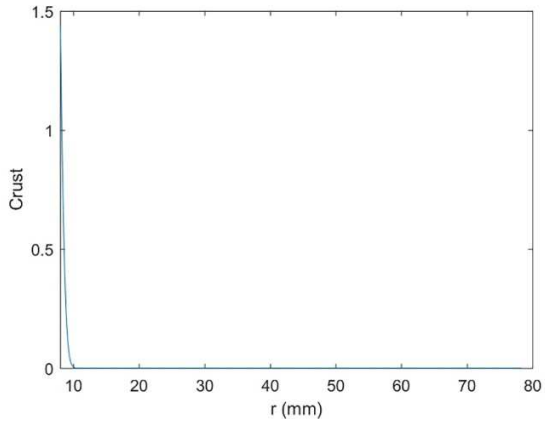

(c)

Figure 8. Modelling Results for Case 3 (a) Interface Pressure vs. Time (b) Interface Pressure vs. Radial Expansion of Concrete (c) Concentration of Rust along the Radius of Concrete

5 Influence Factors of the Modelling

The chemo-mechanical coupled model has been tested and partially validated. From the results, one can conclude that varies parameters affect the crack formation process. Here we conduct a parametric study of thickness of the cement surrounding, corrosion current density, volume ratios of the corrosion product, tensile strength of the cement, and the elastic moduli using this model.

At first, the influence of the thickness of cement sheath is considered. To study this effect for different thicknesses, the inner radius of the cement was fixed at 8 mm and the outer radius at 34.88 mm, 56 mm, and 78.30 mm. The results are shown in Figure 9 below.

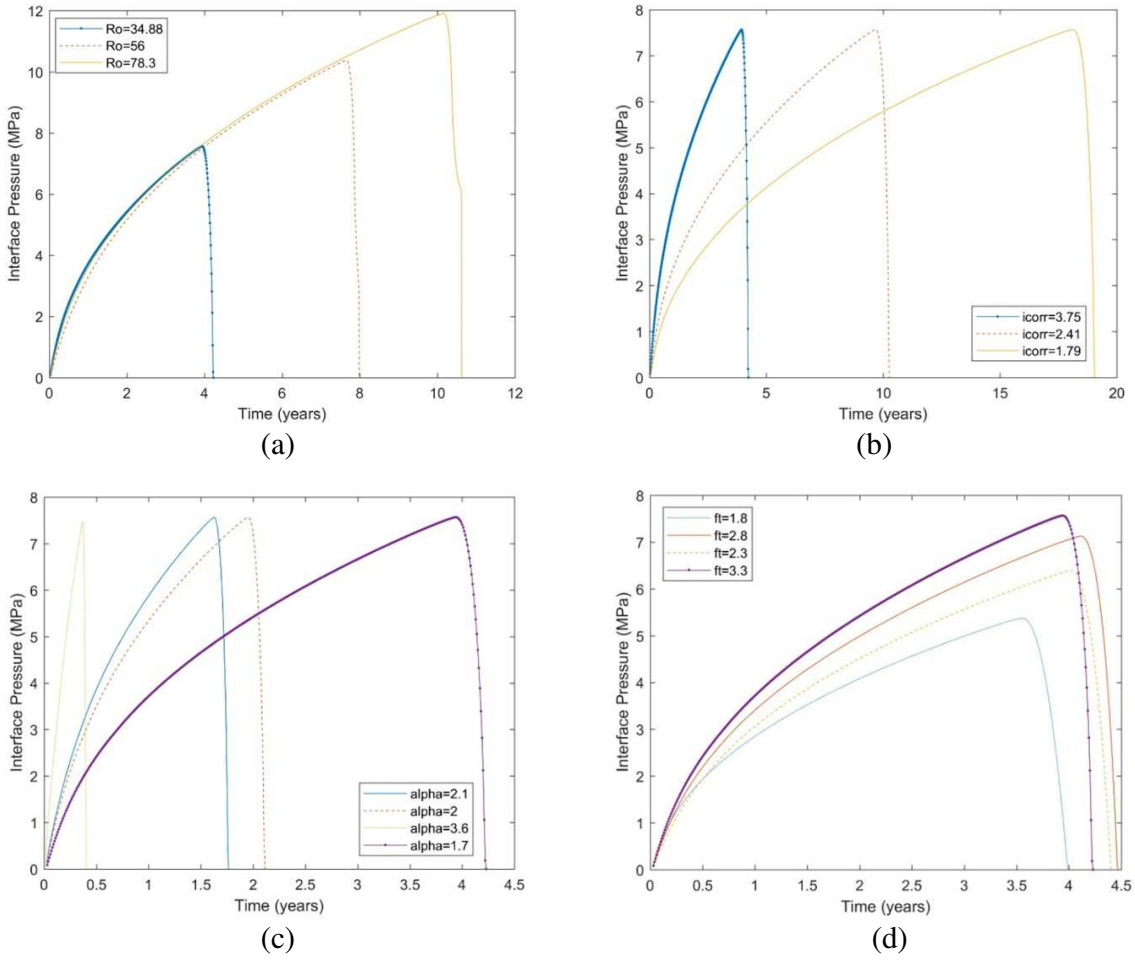

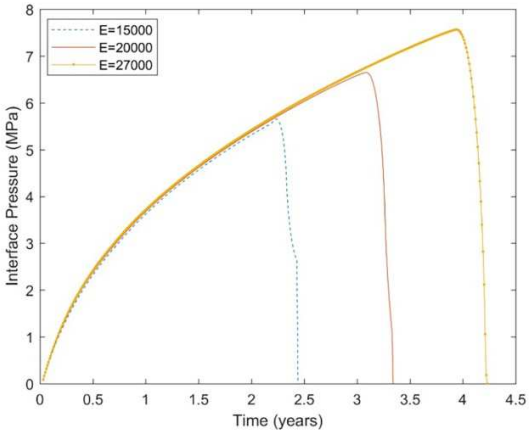

(e)

Figure 9. Simulation Results from Different Influence Factors (a) Thickness of the Cement Surrounding (b) Corrosion Current Density (c) Volume Ratios of the Corrosion Product (d) Tensile Strengths of the Cement (e) Elastic Moduli

From the Figure 9(a), it can be seen that with the increase of thickness of the cement surrounding, both the time of cracking would occur earlier, and accumulation of interface pressure would be increased, which means the thicker cement surrounding would have a longer lifetime.

The next parameter that was considered is the corrosion current density. From literature, one can see that this parameter is not a constant. It is mainly affected by the chemical composition of the metal [32]. From the result shown in Figure 9(b), it can be concluded that the different corrosion current densities had a large effect on the lifetime of the surrounding cement. When the value of the corrosion current density is lower, the lifetime of cement is longer. The corrosion current density did not have any influence on the peak value of the interface pressure.

The next influence factor considered here is the volume ratio of the corrosion product, which is shown in Table 2. Different volume ratios of the corrosion product are compared in Figure 9(c). From the figure, it can be concluded that with the increase of the volume ratio of the corrosion product, the lifetime of cement surrounding is shorter (FeO > Fe_3O_4 > Fe_2O_3 > $Fe(OH)_2$). Similarly, the volume ratio of corrosion product does not affect the peak value of interface pressure.

Two other influence factors are the tensile strength and elastic modulus of the cement, which can be discussed together since they are both the material parameters for the surrounding cement. The influence of tensile strength of cement is complicated. When the tensile strength increases from 1.8 to 2.8 MPa, both the time to crack and the interface pressure increase. However, when the tensile strength continues increasing up to 3.3 MPa, the cracking time is even shorter compared to a tensile strength of 2.8 MPa. Therefore, it can be concluded that there should be a critical value of tensile strength which can effectively extend the lifetime of cement surrounding. In addition, from Figure 9(e), the difference among elastic modulus shows a clear trend that with the increase of the elastic moduli, both peak value of interface pressure and the lifetime of the cement surrounding would increase.

6 Application of Model to Well Cement

To apply the model to a well environment, Class G cement properties are determined experimentally, and realistic dimensions are introduced.

A borehole system was applied in the model with inner radius of 51 mm and an outer radius of 151 mm. The thickness of the steel pipe is 38 mm. For the model, the material parameters needed are fracture energy, tensile strength, elastic modulus, and the porosity of the cement. These three parameters are determined experimentally. Class G cement samples are cast following the API 10A standard.

The elastic modulus of the Class G cement can be derived from a compression test [33]. Then, the elastic modulus can be calculated with Equation 44 assuming the ascending part of the stress-strain curve is linear.

$$E = \frac{f_c}{\varepsilon} \qquad (44)$$

where E is the elastic modulus of the well cement, f_c is the compressive strength of the Class G cement, and ε is the strain corresponding to f_c.

The fracture energy can be derived from the fracture test. The three-point bending test of the notched cement beam is in accordance with the ASTM Standards [34]. According to the data obtained from the test and the calculation method from the ASTM standard, the fracture toughness K_{IC} equals 0.88 ($Mpa \cdot m^{0.5}$). After that, the fracture energy can be derived from the fracture strength found in Equation 45.

$$G_c = \frac{{K_{IC}}^2}{E} \qquad (45)$$

where K_{IC} is the fracture strength, and G_c is the fracture energy of the well cement.

The tensile strength of the well cement can be measured by the splitting tension test [35]. Cylinder samples were prepared and cured for 28 days. The porosity of the well cement can be measured using the method determined by ASTM C830 [36]. The porosity of well cement can be calculated using Equation 46.

$$Porosity = \frac{\frac{W_{SSD} - W_{OD}}{\rho_{water}}}{V_{sample}} \qquad (46)$$

where W_{SSD} is the weight of sample under saturated surface dry condition, W_{OD} is the weight of sample under oven dry condition, V_{sample} is the volume of sample, and ρ_{water} is the density of water.

All parameters for the well cement are listed in Table 5. The values for normal concrete are also included as comparison. One can see that for the same porosity, well cement has a lower tensile strength and elastic modulus, and higher fracture energy. Using these parameters, the theoretical modelling work was applied to the oil well cement. The prediction results are shown in Figures 10 to 14.

Table 5 Comparison of the Changed Parameters.

	Fracture Energy (N/mm)	Elastic Modulus (MPa)	Tensile Strength (MPa)	Porosity (%)
Well Cement	0.0863	8968.5	2.38	40
Concrete	0.02	27000	3.3	40

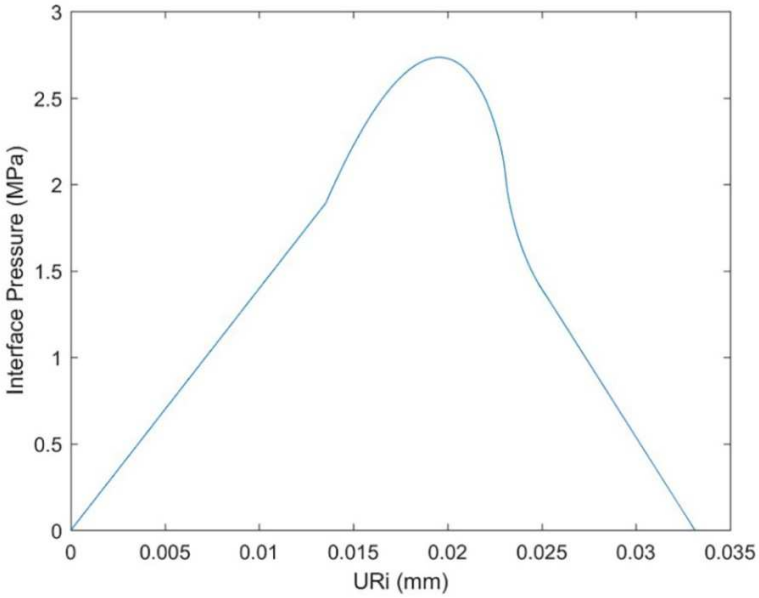

514
515 **Figure 10.** Interface Pressure vs. Radial Displacement
516

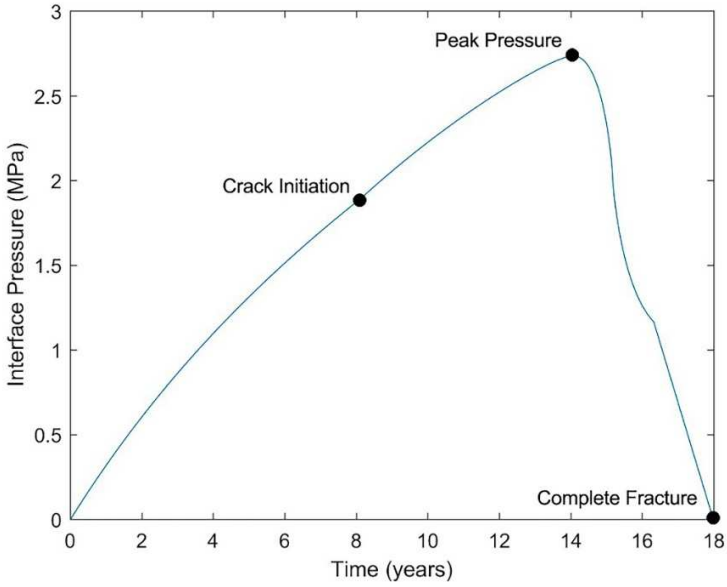

517
518 **Figure 11.** Interface Pressure vs. Time
519

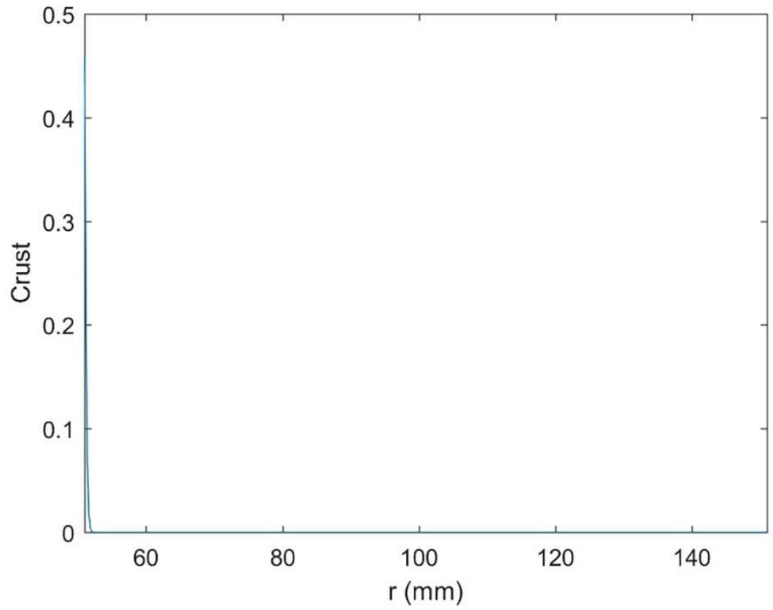

Figure 12. Concentration of Rust before Completely Crack (17.98 years)

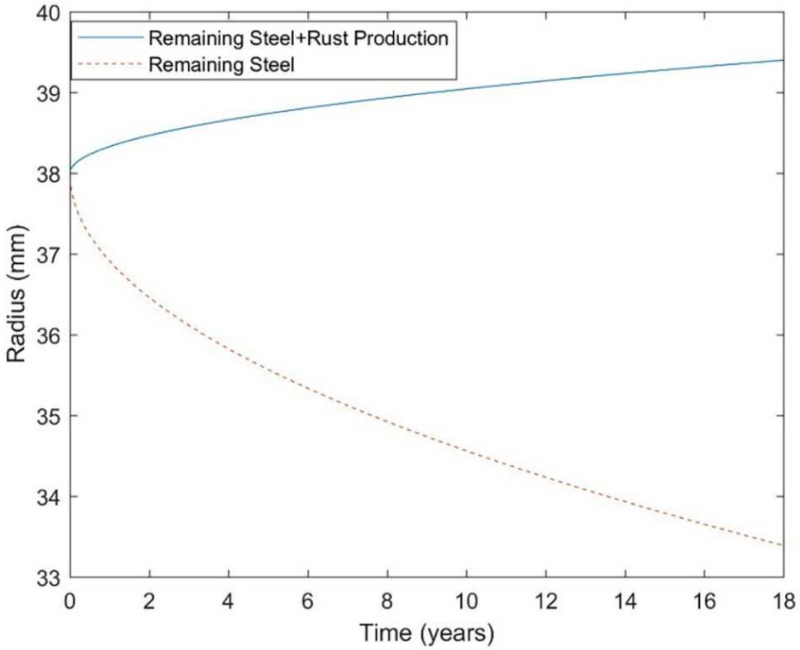

Figure 13. Steel Pipe Radius vs. Time

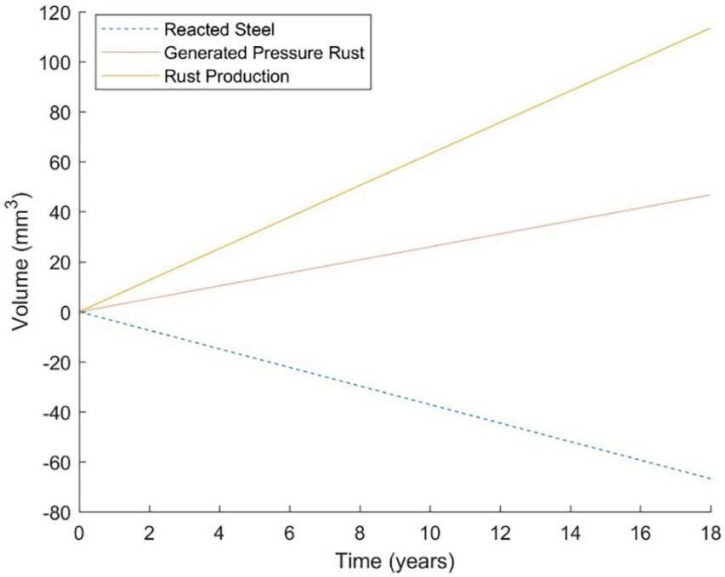

Figure 14. Volume Change for Rust and Steel Pipe

From Figure 10, one can see that with the increase of interface pressure, the radial displacement also increases. This is due to the formation of the large amount of rust, which results in increased radial displacement. The curve can be divided into three parts. The first part is the linear elastic part. During this part, there are no cracks in the cement. The interface pressure is totally resisted by the cement surroundings which behaves linearly. The beginning of the second stage is the top point shown in Figure 10, which shows a slope change. This point is the starting point of the nonlinear elastic part. During this period, the crack starts to form and propagate. The slope of the curve in the second portion gradually decreases until it reaches a peak, which is the starting point of the third section. After the peak point, the interface pressure starts to decrease, and rapidly approaches zero, indicating that the crack propagation period is quick, and the resistance is weak. A similar trend appeared with interface pressure vs. time, shown in Figure 11. Figure 12 shows the concentration of rust. As discussed above, the diffusion coefficient "*k*" is relatively low, which makes it hard for the rust to penetrate.

Figure 13 and Figure 14 describe the volume change of steel due to the rust formation. The volume of steel decreased linearly due to the linear corrosion rate used in the model. However, the net volume increased due to the generated rust. This is because the volume of rust is larger than the original volume of the steel. It is the reason why the rust formation results in interface pressure. As mentioned in Section 2.1, not all the rust directly contributes to the interface pressure causing cracking of well cement. Part of the rust production will first fill the space left by the corroded steel, fill the interface transition zone (ITZ) between the steel casing and the surrounding well cement, and fill some pores in the well cement. The excess rust will produce the interface pressure.

Table 6 Timeline of Cracking.

Condition	Time (years)
Crack Initiation	8.12
Peak Pressure	14.09

Completely Fracture	17.98

Table 6 shows the prediction of cracking by the model prediction under one set of input data. Compared to previous cases, a larger borehole system would not greatly affect the lifetime of the cement surrounding. The material parameters are the main influence factors to be considered. Since mechanical properties of Class G cement differ from normal concrete, the time to crack completely is shorter. However, because of its prominent fluidity, it can be used to replace concrete in the field.

7 Conclusions

The potential lifespan of well cement surrounding the steel casing in the borehole system underground has been simulated by using a chemo-mechanical coupled model. This paper mainly focuses on the impact of steel corrosion on well cement. The rate of rust production was predicted and the effect of the generated pressure by the rust on the interface of steel pipe and surrounding well cement was calculated. The penetration of rust into surrounding well cement was captured by using Darcy's law. When the interface pressure is larger than the tensile strength of the cement, the well cement cracks. From crack initiation in the well cement to a complete fracture of the surrounding well cement, the process was predicted with the Fictitious Crack Model. Additionally, several important points are concluded below:

(1) The time to the first cracking of well cement can be effectively predicted using the model calibrated based on previous experimental work.

(2) The modelling results are highly dependent on input parameters, especially the material parameters of well cement and steel pipe, and the size of the borehole system.

(3) The material properties of Class G cement were experimentally obtained and used in the model.

(4) The diffusion coefficient of rust was assumed as a small value, and thus, the diffusion level of rust is low. Further experimental study is needed to verify the diffusion coefficient of rust in well cement.

(5) This chemo-mechanical coupled model can successfully predict the general trend of rust formation, generation of interface pressure, and the cracking mechanism for a steel casing surrounded by well cement in an underground borehole system.

Acknowledgements

This work was supported by the U.S. Department of Energy (project Nanoparticle Injection Technology for Remediating Leaks of CO_2 Storage Formation, DE-FE0026514).

Data Availability Statement

The raw/processed data required to reproduce these findings cannot be shared at this time as the data also forms part of an ongoing study.

595 **References**

596 [1] O. Poupard, V. L'Hostis, S. Catinaud, I. Petre-Lazar, Corrosion damage diagnosis of a
597 reinforced concrete beam after 40 years natural exposure in marine environment, Cem.
598 Concr. Res. 36 (2006) 504–520. doi:10.1016/j.cemconres.2005.11.004.

599 [2] G. H. Koch, M. P. H. Brongers, N. G. Thompson, Y. P. Virmani, J. H. Payer, Corrosion
600 Cost and Preventive Strategies in the United States, FHWA, 2001.

601 [3] U. Angst, B. Elsener, C.K. Larsen, Ø. Vennesland, Critical chloride content in reinforced
602 concrete - A review, Cem. Concr. Res. 39 (2009) 1122–1138.
603 doi:10.1016/j.cemconres.2009.08.006.

604 [4] S. Ahmad, Reinforcement corrosion in concrete structures, its monitoring and service life
605 prediction - A review, Cem. Concr. Compos. 25 (2003) 459–471.
606 doi:10.1016/S0958-9465(02)00086-0.

607 [5] E. Rozière, A. Loukili, F. Cussigh, A performance based approach for durability of concrete
608 exposed to carbonation, Constr. Build. Mater. 23 (2009) 190–199.
609 doi:10.1016/j.conbuildmat.2008.01.006.

610 [6] Y. Xi, N. Abu-Hejleh, A. Asiz, A. Suwito, Performance Evaluation of Various Corrosion
611 Protection Systems of Bridges in Colorado, 2004.
612 http://www.dot.state.co.us/publications/CorrosionProtection/CorrosionProtection.pdf.

613 [7] J.N. Enevoldsen, C.M. Hansson, B.B. Hope, The influence of internal relative humidity on
614 the rate of corrosion of steel embedded in concrete and mortar, Cem. Concr. Res. 24 (1994)
615 1373–1382. doi:10.1016/0008-8846(94)90122-8.

616 [8] K.D. Stanish, R.D. Hooton, M.D. Thomas, Testing the Chloride Penetration Resistance of
617 Concrete: A Literature Review, FWHA, 1997. doi:10.1016/j.jfoodeng.2008.09.025.

618 [9] R.J. Detwiler, K.O. Kjellsen, O.E. Gjory, Resistance to chloride intrusion of concrete cured
619 at different temperatures, Mater. J. 88 (1991) 19–24. doi:10.14359/2326.

620 [10] Y. Xi, A. Ababneh, Prediction of the Onset of Steel Corrosion in Concrete by Multiscale
621 Chloride Diffusion, in: Int. Sym., 2000: pp. 181–186.

622 [11] G. Frigione, Gypsum in Cement, Pergamon Press Ltd., 1983.
623 doi:10.1016/B978-0-08-028670-9.50020-X.

624 [12] C. Suwito, Y. Xi, The effect of chloride-induced steel corrosion on service life of reinforced
625 concrete structures, Struct. Infrastruct. Eng. 4 (2008) 177–192.
626 doi:10.1080/15732470600688699.

627 [13] K. Tuutti, Corrosion of steel in concrete, Swedish Cement and Concrete Research Institute,
628 1982.

629 [14] P.D. Cady, R.E. Weyers, Chloride Penetration and the Deterioration of Concrete Bridge
630 Decks, Cem. Concr. Aggregates. 5 (1983) 81–87. doi:10.1520/CCA10258J.

631 [15] P. Thoft-Christensen, Corrosion and Cracking of Reinforced Concrete, in: Third Int.
632 IABMAS Work. Life- Cycle Cost Anal. Des. Civ. Infrastructures Syst. JCSS Work.
633 Probabilistic Model. Deterior. Process. Concr. Struct., 2003: pp. 26–36.

634 [16] K. Luke, A. Torres, G. Quercia Bianchi, POROSITY MEASUREMENT OF HYDRATED
635 OIL WELL CEMENTS, in: Thirty-Seventh Int. Conf. Cem. Microsc., 2015: pp. 250–262.

636 [17] Z. P. Bažant, Physical model for steel corrosion in concrete sea structures—theory, Journal
637 of the Structural Division 105 (1979) 1137–1153.

638 [18] B.B. Hope, J.A. Page, A.K.C. Ip, Corrosion Rates of Steel in Concrete, Cem. Concr. Res. 16
639 (2011) 771–781. doi:10.1016/0008-8846(86)90051-7.

640 [19] S.C. Kranc, A.A. Sagues, Computation of reinforcing steel corrosion distribution in
641 concrete marine bridge substructures, Corrosion. 50 (1994) 50–61. doi:10.5006/1.3293494.

642 [20] D.P. Bentz, E.J. Garboczi, Simulation studies of the effects of mineral admixtures on the
643 cement paste-aggregate interfacial zone, ACI Mater. J. 88 (1991) 518–529.

644 [21] S. Timoshenko, Strength of Materials: Part II, Advanced Theory and Problems, D. Van
645 Nostrand Company, 1956.

646 [22] Z.P. Bažant, Size Effect in Blunt Fracture: Concrete, Rock, Metal, J. Eng. Mech. 110 (1984)
647 518–535. doi:10.1061/(ASCE)0733-9399(1984)110:4(518).

648 [23] A. Hillerborg, M. Modéer, P.E. Petersson, Analysis of crack formation and crack growth in
649 concrete by means of fracture mechanics and finite elements, Cem. Concr. Res. 6 (1976)
650 773–781. doi:10.1016/0008-8846(76)90007-7.

651 [24] Z.P. Bažant, Concrete fracture models: testing and practice, Eng. Fract. Mech. 69 (2002)
652 165–205. doi:10.1016/S0013-7944(01)00084-4.

653 [25] G. Rosati, C. Schumm, Modeling of local bar-to-concrete bond in reinforced concrete
654 beams, in: Int. Conf. Bond Concr., 1992: pp. 34–43.

655 [26] K. Noghabai, Effect of tension softening on the performance of concrete structures:
656 experimental, analytical and computational studies, Lulea University of Technology, 1998.

[27] S.J. Pantazopoulou, K.D. Papoulia, Modeling Cover -Cracking Due To Reinforcement Corrosion in Rc S Tructures, J. Eng. Mech. 127 (2001) 342–351. doi:10.1061/(ASCE)0733-9399(2001)127.

[28] E.J. Hansen, V.E. Saouma, Numerical simulation of reinforced concrete deterioration: Part II - Steel corrosion and concrete cracking, ACI Mater. J. 96 (1999) 331–338. doi:10.7575/aiac.ijalel.v.5n.5p.109.

[29] K. Lundgren, Modelling the splitting effects of corrosion in reinforced concrete, in: Comput. Model. Concr. Struct. Euro-C Conf., 2003: pp. 491–500.

[30] Y. Liu, and R.E. Weyers, Modeling the Time-to-Corrosion Cracking in Chloride Contaminated Reinforced Concrete Structures, Mater. J. 95 (n.d.). doi:10.14359/410.

[31] C. Andrade, D. Whiting, A comparison of chloride ion diffusion coefficients derived from concentration gradients and non-steady state accelerated ionic migration, October. 29 (1996) 476–484. doi:10.1007/BF02486282.

[32] ASTM G102-89-15 Standard Practice for Calculation of Corrosion Rates and Related Information from Electrochemical Measurements, ASTM International, West Conshohocken, PA, 2015, https://doi.org/10.1520/G0102-89R15E01.

[33] ASTM C469/C469M-14 Standard Test Method for Static Modulus of Elasticity and Poisson's Ratio of Concrete in Compression, ASTM International, West Conshohocken, PA, 2014, https://doi.org/10.1520/C0469_C0469M-14.

[34] ASTM E1290-99 Standard Test Method for Crack-Tip Opening Displacement (CTOD) Fracture Toughness Measurement, ASTM International, West Conshohocken, PA, 1999, https://doi.org/10.1520/E1290-99.

[35] ASTM C496/C496M-17 Standard Test Method for Splitting Tensile Strength of Cylindrical Concrete Specimens, ASTM International, West Conshohocken, PA, 2017, https://doi.org/10.1520/C0496_C0496M-17.

[36] ASTM C830-00(2016) Standard Test Methods for Apparent Porosity, Liquid Absorption, Apparent Specific Gravity, and Bulk Density of Refractory Shapes by Vacuum Pressure, ASTM International, West Conshohocken, PA, 2016, https://doi.org/10.1520/C0830-00R16.